3D Microwave Tomography with Huber Regularization Applied to Realistic Numerical Breast Phantoms

Funing Bai[1], Ann Franchois[2, *], and Aleksandra Pižurica[1]

Abstract—Quantitative active microwave imaging for breast cancer screening and therapy monitoring applications requires adequate reconstruction algorithms, in particular with regard to the nonlinearity and ill-posedness of the inverse problem. We employ a fully vectorial three-dimensional nonlinear inversion algorithm for reconstructing complex permittivity profiles from multi-view single-frequency scattered field data, which is based on a Gauss-Newton optimization of a regularized cost function. We tested it before with various types of regularizing functions for piecewise-constant objects from Institut Fresnel and with a quadratic smoothing function for a realistic numerical breast phantom. In the present paper we adopt a cost function that includes a Huber function in its regularization term, relying on a Markov Random Field approach. The Huber function favors spatial smoothing within homogeneous regions while preserving discontinuities between contrasted tissues. We illustrate the technique with 3D reconstructions from synthetic data at 2 GHz for realistic numerical breast phantoms from the University of Wisconsin-Madison UWCEM online repository: we compare Huber regularization with a multiplicative smoothing regularization and show reconstructions for various positions of a tumor, for multiple tumors and for different tumor sizes, from a sparse and from a denser data configuration.

1. INTRODUCTION

Microwave biomedical imaging relies on the capability of microwaves to differentiate among tissues based on the contrast in their dielectric properties. It is currently being investigated as an alternative or complementary imaging modality to X-ray mammography for breast cancer screening and/or therapy monitoring. Malignant-to-normal tissue contrasts of various degrees have been reported [1, 2] and are ascribed to tumors having a higher water content, hence higher relative permittivity and conductivity values, than normal tissues. Benefits of microwave breast imaging such as its non-ionizing nature and moderate cost have stimulated research in this field over the last two decades. Promising clinical 3D tomographic images are shown in [3] for a screening example of a 1.2 cm sized tumor and for a monitoring example.

An active microwave imaging system mainly consists of a transmit-receive antenna setup for illuminating the target and collecting the scattered microwave field data and a reconstruction algorithm for processing these data to an image. The focus in this paper is on the latter. Let us recall some early biomedical experiments that yielded two-dimensional (2D) transmission coefficient images [4] and 2D diffraction tomography (DT) images [5] of *ex-vivo* animal kidneys as well as 2D-DT images of an *in-vivo* human forearm [6]. Qualitative approaches also have been proposed, more recently, for breast cancer imaging, including ultra-wideband synthetic focusing techniques [7–9] and a linear sampling technique [10]. Since the nineties quantitative reconstruction algorithms based on rigorous solutions of Maxwell's equations have been developed to provide images of the complex permittivity profile, see,

[1] Department of Telecommunications and Information Processing (IPI-TELIN-Iminds), Ghent University, Ghent B-9000, Belgium.
[2] Department of Information Technology (INTEC), Ghent University, Ghent B-9000, Belgium.

e.g., [11–16] for 2D and [13, 16–19] for 3D frequency-domain techniques and [20–22] for time-domain (TD) techniques. These algorithms have been tested with biomedical experimental data, e.g., for various biological phantoms [16, 22–24] and a human forearm [16, 25, 26] in 2D, for plastic rods in saline [27] in pseudo-3D, for a canine thorax [28] in a 3D scalar approximation and for dielectric balls [29] and a pig hind-leg [30] in fully-vectorial 3D. Quantitative imaging of the breast is reported, e.g., employing 2D single-frequency algorithms with synthetic data [26, 31] or with phantom and/or clinical data [32–34], a 3D single-frequency algorithm in a scalar approximation with synthetic data [35], a 3D TD algorithm with synthetic and phantom data [36], a 3D multiple-frequency vectorial algorithm with synthetic data [37–40] and 3D single-frequency fully vectorial algorithms with synthetic data [41–43] and with single-polarized clinical data [3]. In this paper we consider a 3D single-frequency fully vectorial imaging algorithm.

Reconstructing the complex permittivity profile is a nonlinear and ill-posed inverse problem. It is solved by letting a nonlinear optimization scheme minimize a data-fit cost function, where some kind of regularization is provided to cope with the ill-posedness. The Gauss-Newton method has been employed for microwave breast imaging by several authors, e.g., [3, 14, 26, 33, 34, 37–45] and it is used in this paper as well. The cost function in [3, 14, 33, 34, 37–40, 44] is the non-regularized data-fit — the method is often referred to as the Distorted Born Iterative Method (DBIM) [11]. Its minimum generally is not well-defined, especially when the number of reconstruction variables is large. In this case a regularization is applied to the permittivity *update* in each iteration of the optimization: Tikhonov regularization — similar to [11, 13] — in [14, 34, 37], a combination of L1 and L2 norm sparsity promoting regularization in [38] and other compressive sensing schemes in, e.g., [44] and a conjugate gradient for least squares (CGLS) algorithm in [3, 33, 39, 40]. In the present paper, as in [26, 42, 43, 45] for microwave breast imaging and as in, e.g., [19, 30, 46–52] for microwave imaging, we adopt a regularized cost function consisting of the data fit term and a regularization term. The regularization term allows for easy incorporation of *a priori* information on the complex permittivity profile. This approach can be interpreted within a Bayesian framework employing Markov Random Fields (MRF), where the energy function is defined as a sum of clique potentials; see for microwave imaging, e.g., [50, 51], where a Gauss-Newton, and [53–55], where other schemes are adopted for the optimization.

Different regularizing functions have been analyzed in the framework of microwave imaging. Quadratic (L2-norm) smoothing regularization [19, 46], or a Tikhonov potential function [53, 55], penalizes small differences between neighboring permittivity values, but also smooths out true discontinuities; it is applied to 3D simulated breast imaging in an additive multiplicative fashion in [43]. For (quasi) piecewise-constant profiles strong edge-preserving capabilities are shown by value picking (VP) regularization [48, 56], which is a nonspatially structured approach, and by piecewise-smoothed VP regularization (a combined nonspatially-spatially structured approach) [49], when applied to measured data from the 3D and 2D Fresnel databases, respectively, but these techniques perform best for a limited number of different permittivity values. Weighted L2-norm total variation (TV) regularization, where the weights are reduced at discontinuities, is applied to biomedical imaging in [16, 26, 30] and to 2D simulated breast imaging in [26]. In [45] a soft prior quadratic regularization that exploits spatial information from alternative imaging modalities (MR or x-ray CT) is successfully applied to 2D breast phantom imaging, but in this paper we do not assume tissue boundaries to be known.

Various edge-preserving potential functions, which smooth the homogeneous areas of an image while preserving edges, without *a priori* knowledge of the edge locations, are employed in [50–54] in a spatially structured regularization; for example, discontinuity adaptive (DA) models [57] turn off smoothing less abruptly than line process [53] and weak membrane [54] models; an advantage of the well-known Huber function [58] is that it is nonquadratic but convex [59]: it consists of a quadratic function for arguments below a threshold, for smoothing small scale noise, and of a linear function above the threshold, for preserving discontinuities. In [50, 51] we tested different DA functions, including the Huber function, with measured scattered field data for 2D and 3D piecewise-constant lossless dielectric targets in air from Institut Fresnel [60, 61]; the Huber function yielded an average reconstruction error of 14.9% for the 2D case (see [50] for the error values and [62, p.78] for a correction in the error formula) — the maximum target-to-background permittivity contrast was 3-to-1; for the 3D case reconstructed permittivities were within 5% of the actual values for the two-spheres and two-cubes targets [51] — with maximum target-to-background contrasts of 2.6- and 2.3-to-1, respectively.

In case of microwave breast imaging the target is lossy and (strongly) inhomogeneous and the tumor-to-background contrast typically is larger than with the aforementioned targets from the Fresnel databases. In the present paper, as in [42] where we reported some preliminary results indicating the potentials of Huber regularization for breast imaging, we adopt a tumor-to-background contrast of 50-to-10 for the real part and of 10-to-2 for the imaginary part of the complex permittivity. We present a more elaborate study here than in [42]: we now consider different realistic numerical breast phantoms, which we derived from two phantoms from the University of Wisconsin-Madison (UWCEM) online repository [63] and we examine the influence of the tumor size and position as well as of multiple tumors on the reconstructions. We also consider the effect of the antenna density on the reconstruction quality. Furthermore, we compare the performance of the Huber regularization with a quadratic smoothing regularization [19].

The paper is organized as follows. The reconstruction algorithm and Huber regularization are briefly discussed in Section 2. In Section 3, the methodology for data generation, the phantoms and antenna configurations are introduced. Results are shown in Section 4. Section 5 concludes the paper.

2. RECONSTRUCTION ALGORITHM

We consider a breast that is immersed in a homogeneous (lossy) medium with known relative complex permittivity ε_b — the rest of the body, an enclosure and antenna coupling are not included in our scattering model. The breast is illuminated successively with different known microwave fields emitted by elementary dipole antennas that are located on a surface surrounding its front side and that can be oriented along different polarizations. For each illumination the scattered field components are measured in receiving locations on the same surface. A single fixed frequency f is adopted and the time dependency $e^{j\omega t}$ of the fields is omitted in the following. Our goal is to reconstruct the relative complex permittivity

$$\varepsilon(\mathbf{r}) = \varepsilon'(\mathbf{r}) - j\frac{\sigma(\mathbf{r})}{\omega\epsilon_0}, \tag{1}$$

where ε' is the relative permittivity and σ the conductivity in every point $\mathbf{r}$ in a cuboidal reconstruction domain $\mathcal{D}$ that contains the breast and is located inside the transmit/receive surface. Below we summarize the Gauss-Newton reconstruction algorithm [19, 43, 48] and briefly describe the Huber regularization [50, 51].

2.1. Gauss-Newton Minimization of a Regularized Cost Function

The unknown relative complex permittivity $\varepsilon(\mathbf{r})$ is discretized in $\mathcal{D}$ on a uniform rectangular grid with N^ε cubic cells, resulting in a N^ε-dimensional vector $\boldsymbol{\varepsilon} = [\varepsilon_1, \ldots, \varepsilon_{N^\varepsilon}]$. We solve the inverse problem for the permittivity vector by iterative minimization of a cost function

$$F(\boldsymbol{\varepsilon}) = F^{LS}(\boldsymbol{\varepsilon}) + \mu F^D(\boldsymbol{\varepsilon}), \tag{2}$$

where $F^D(\boldsymbol{\varepsilon})$ denotes the regularization function, μ is a positive regularization parameter and

$$F^{LS}(\boldsymbol{\varepsilon}) = \frac{\|\mathbf{e}^{meas} - \mathbf{e}^{scat}(\boldsymbol{\varepsilon})\|^2}{\|\mathbf{e}^{meas}\|^2} \tag{3}$$

is the normalized least squares data error, with $\|\cdot\|$ the L2 norm. In Eq. (3), $\mathbf{e}^{meas}$ and $\mathbf{e}^{scat}(\boldsymbol{\varepsilon})$ are N^d-dimensional vectors that contain the measured scattered field components (complex numbers) for all used combinations of transmitters and receivers and the corresponding computed scattered field components for a given permittivity vector $\boldsymbol{\varepsilon}$, respectively. Note that the scattered field is defined as the total field (with the breast in place) minus the incident field (the breast is not present). For the computation of $\mathbf{e}^{scat}(\boldsymbol{\varepsilon})$, i.e., the forward problem solution, we use a fast BiCGSTAB-FFT fully vectorial forward solver, see [19, 64] for details, which is based on a Method of Moments discretization of a mixed potential volume integral equation for the electric flux density in $\mathcal{D}$ and on a BiCGSTAB-FFT iterative solution of the resulting linear system, where the initial field is chosen with a "marching on in source position" technique. Note that the discrete dipole approximation (DDA) in [3, 65] leads to a similar discretization.

For the minimization of Eq. (2) we employ the (independent) variables ε_ν and ε_ν^*, with $(.)^*$ the complex conjugate, and we apply a Gauss-Newton technique, meaning here that the second order derivatives $\frac{\partial^2 F}{\partial \varepsilon_\nu \partial \varepsilon_{\nu'}}$ and $\frac{\partial^2 F}{\partial \varepsilon_\nu^* \partial \varepsilon_{\nu'}^*}$ in the complex Hessian matrix of the Newton update formula are neglected. The resulting Gauss-Newton update $\mathbf{s}_k$ at iteration k is used as a search direction and satisfies the equation [48]

$$\left(\mathbf{J}_k^H \mathbf{J}_k + \lambda^2 \mathbf{\Sigma}_k^D\right) \mathbf{s}_k = -(\mathbf{J}_k^H[\mathbf{e}^{scat}(\varepsilon_k) - \mathbf{e}^{meas}] + \lambda^2 \mathbf{\Omega}_k^{D*}), \tag{4}$$

where $(.)^H$ stands for Hermitian transpose. The trade-off parameter λ is given by $\lambda^2 = \mu\|\mathbf{e}^{meas}\|^2$. The $N^d \times N^\varepsilon$ matrix $\mathbf{J}$ is the Jacobian matrix, $\mathbf{\Omega}^{D*}$ is a N^ε-dimensional vector with first order derivatives and $\mathbf{\Sigma}^D$ a $N^\varepsilon \times N^\varepsilon$ matrix with second order derivatives of $F^D(\varepsilon)$. In this paper, the update system (4) is solved with a BiCGSTAB solver [66] (a subspace preconditioned LSQR method [43] is used when MS regularization is applied).

The new permittivity vector ε_{k+1} is then obtained by performing an approximate minimization [67] of the cost function $F(\varepsilon_{k+1}(\beta))$ along a chosen path with parameter β. Usually, as, e.g., in [19], a line-search is performed along the Gauss-Newton update direction, i.e., $\varepsilon_{k+1} = \varepsilon_k + \beta_k \mathbf{s}_k$. In this paper we employ the constrained search path from [43], which smoothly incorporates lower and upper bounds on the real and imaginary parts of the complex permittivity.

2.2. Huber Regularization

It is well known that the MRF provides a convenient and consistent way of modeling the global context in terms of local interactions between image entities (pixels, voxels, segments, etc.) [57]. We define the regularizing function $F^D(\varepsilon)$ as

$$F^D(\varepsilon) = \frac{1}{2} \sum_\nu \sum_{\nu' \in N_\nu} g(\varepsilon_\nu - \varepsilon_{\nu'}), \tag{5}$$

where g is a potential function and N_ν the neighborhood of ν. We use 26 neighbors in 3D. Let $\eta = \varepsilon_\nu - \varepsilon_{\nu'}$ denote the difference between two neighboring complex permittivities. The Huber function g_h with threshold parameter γ is defined as [50, 51]

$$g_h(\eta) = \begin{cases} |\eta|^2 & |\eta| \leq \gamma, \\ 2\gamma|\eta| - \gamma^2 & otherwise. \end{cases} \tag{6}$$

The model of Eq. (6) can be considered as a 2D extension of the 1D Huber model [57–59] and yields bounded smoothing. The expressions for the first and second order derivatives of Eq. (5) with the potential function in Eq. (6) are [50, 51]

$$\mathbf{\Omega}^{D*} = \frac{\partial F^D}{\partial \varepsilon_\nu^*} = \sum_{\nu' \in N_\nu} \omega_{\nu'}, \tag{7}$$

$$\Sigma_{\nu,\nu}^D = \frac{\partial^2 F^D}{\partial \varepsilon_\nu \partial \varepsilon_\nu^*} = \sum_{\nu' \in N_\nu} \sigma_{\nu'}, \tag{8}$$

$$\Sigma_{\nu,\nu'}^D = \frac{\partial^2 F^D}{\partial \varepsilon_{\nu'} \partial \varepsilon_\nu^*} = -\sigma_{\nu'} \; for \; \nu' \in N_\nu \tag{9}$$

Table 1. Expressions for $\omega_{\nu'}$ and $\sigma_{\nu'}$ for the Huber function.

	$|\varepsilon_\nu - \varepsilon_{\nu'}| \leq \gamma$	otherwise
$\omega_{\nu'}$	$(\varepsilon_\nu - \varepsilon_{\nu'})$	$\frac{\gamma(\varepsilon_\nu - \varepsilon_{\nu'})}{|\varepsilon_\nu - \varepsilon_{\nu'}|}$
$\sigma_{\nu'}$	1	$\frac{\gamma}{2|\varepsilon_\nu - \varepsilon_{\nu'}|}$

and $\Sigma^D_{\nu,\nu'} = 0$ for $\nu' \notin N_\nu$, where expressions for $\omega_{\nu'}$ and $\sigma_{\nu'}$ are given in Table 1.

In Section 4 we compare Huber regularization with Multiplicative Smoothing (MS) regularization (a slightly different implementation than in [19] is used here). With MS regularization the cost function is given by $F(\varepsilon) = F^{LS}(\varepsilon)(1 + \mu F^R(\varepsilon))$, where F^R is as (5), with g the Tikhonov function $g_T(\eta) = |\eta|^2$, with 6 nearest neighbors in N_ν — 3 nearest neighbors are used in [19] — and without the fore factor $\frac{1}{2}$.

3. SYNTHETIC DATA GENERATION

The 3D complex permittivity breast phantoms in this paper are adapted from the UWCEM online numerical breast phantoms repository [63]. This repository provides anatomically realistic MRI-derived phantoms, which capture the structural heterogeneity of normal breast tissue and which incorporate the realistic dispersive dielectric properties of normal breast tissue from 0.5 to 20 GHz [68]. We chose a frequency of 2 GHz [62]. Since the high resolution of these phantoms (cell size 0.5 mm) is computationally demanding for the forward problem solution, we derived coarser phantoms (cell size 2.5 mm) for the synthetic data generation. These data are computed with the fully vectorial forward solver [64], where the tolerance for the BiCGSTAB routine is set to 10^{-3}. Let us define the signal-to-noise ratio as

$$\text{SNR} = 10\log_{10}\frac{||e^{meas}||^2}{2N^d\sigma^2}\,\text{dB}, \tag{10}$$

where σ^2 is the variance of additive white Gaussian noise. We set a SNR of 20 dB (10% noise) for all scattered field data that are inverted in this paper. This value lies in the range of SNRs that were estimated with our MS regularized reconstruction algorithm for a number of 3D Fresnel data, i.e., (14–19 dB) in [56] and (23–30 dB) in [19]. The phantoms and antenna configurations are detailed below.

### 3.1. Realistic Numerical Breast Phantoms

We selected two phantoms: phantom 1 (ID 071904) from ACR class 1, which is a mostly fatty breast phantom with some glandular and fibro-connective inhomogeneities, and phantom 3 (ID 010204) from ACR class 2 with a scattered fibroglandular density. Sagittal slices through these full-resolution phantoms at 2 GHz are depicted in Fig. 1. We adapted the phantoms as follows: the permittivity of the background medium is chosen as $\varepsilon_b = 10.0 - j2.0$ ($\sigma_b = 0.223\,\text{S/m}$) [10, 43]; the background wavelength then is $\lambda_b = 4.72\,\text{cm}$; the muscle layer at the chest wall [68] is removed; coarser permittivity phantoms with a cell size 2.5 mm ($= \lambda_b/19$) are obtained by local averaging. Furthermore, we inserted one or more spherical tumors with permittivity $50.0 - j10.0$ [10, 43] and a diameter in the range 2 cm to 1.2 cm, which is smaller than the half-wavelength $\lambda_b/2 = 2.36\,\text{cm}$. Two of these coarser phantoms, with a tumor located at $(3\,\text{cm}, -3\,\text{cm}, 0\,\text{cm})$, are depicted in Fig. 2, showing sagittal (xy-)slices near $z = 0$ and coronal (yz-)slices through the tumor near $x = 3\,\text{cm}$.

3.2. Antenna Configurations

We chose a sparse antenna configuration as in Fig. 3 for the reconstructions in Sections 4.1–4.3, sparse meaning here that the number of nonredundant data is much lower than the number of reconstruction variables. The computational grid (gray cuboid) contains the breast phantom with its chest wall located in the yz facet with $x > 0$ (e.g., at $x = 6\,\text{cm}$ in Fig. 3). The antennas are positioned on 5 circles on a hemi-ellipsoidal-like surface around the cuboid. These circles are centered on the x-axis and parallel to the yz-plane; the first circle is at $x = -10\,\text{cm}$, in front of the nipple, and the last circle is at $x = 7.5\,\text{cm}$. Each circle contains 8 equally spaced antenna positions. The spacing between the largest circles is 5 cm ($\approx 1.1\lambda_b$) and the spacing between the antenna positions on the largest circle (diameter 20 cm) is approximately 7.8 cm ($\approx 1.6\lambda_b$). In each of the 40 positions there are 2 dipoles with polarizations in orthogonal directions. This yields a total of 80 dipoles, which is half of the number used in [43]. All 80 dipoles are used to sample the field, but only the 64 dipoles (indicated with green markers) on the four largest circles are used to illuminate the phantom. This yields a total of $N^d = 5120$ complex field values. Note that due to reciprocity $496 \times 4 = 1984$ of these data values are redundant, which is the
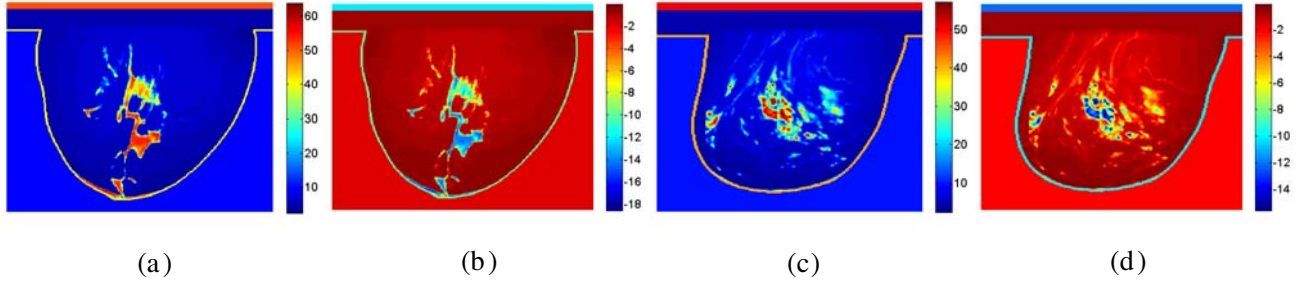
Figure 1. The complex permittivity in a sagittal slice through the full-resolution UWCEM breast phantoms at 2 GHz: (a), (b) class 1 phantom and (c), (d) class 2 phantom. (a), (c) Real part and (b), (d) imaginary part.
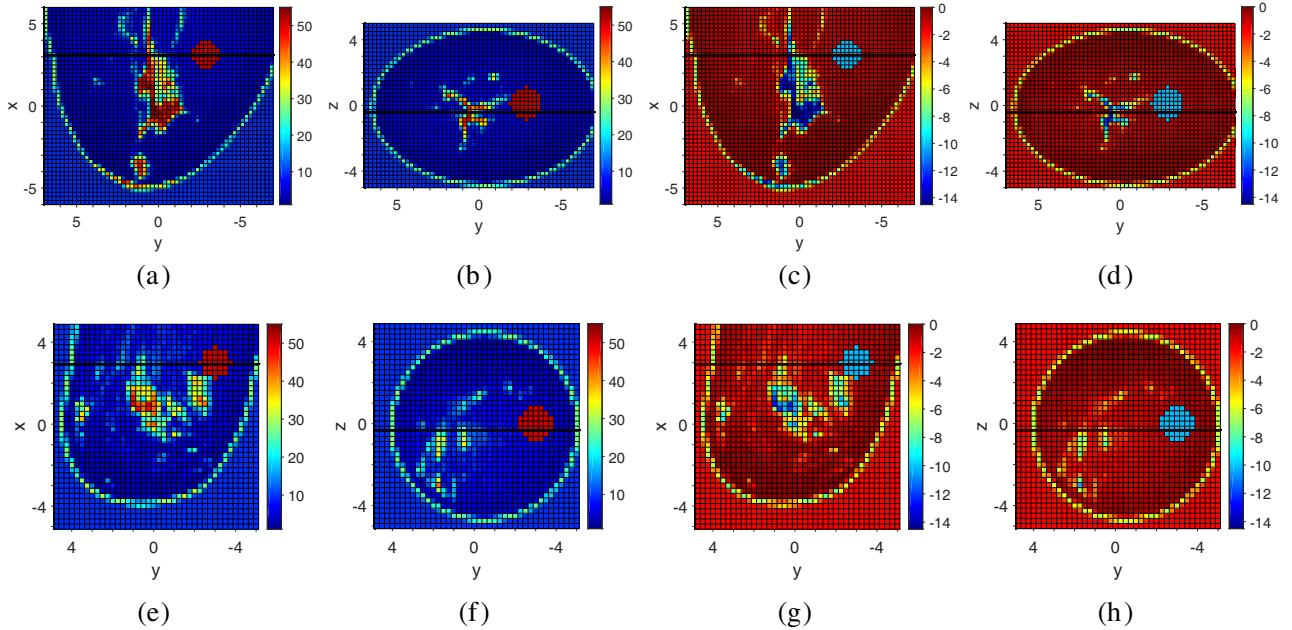
Figure 2. The complex permittivity in slices through the discretized (a)–(d) class 1 phantom and (e)–(h) class 2 phantom used for synthetic data generation. (a), (c), (e), (g) Sagittal slice near $z = 0$ cm and (b), (d), (f), (h) coronal slice near $x = 3$ cm. (a), (b), (e), (f) Real part and (c), (d), (g), (h) imaginary part. A horizontal black line indicates the intersection of sagittal and coronal slices. A spherical tumor is centered at $(3 \text{ cm}, -3 \text{ cm}, 0 \text{ cm})$, with a diameter of 2.0 cm for the class 1 phantom and of 1.6 cm for the class 2 phantom. The cell size is 2.5 mm. Axes are in cm.

number of transmitter position pairs, C_{32}^2, times the number of data values per transmitter position, hence the number of nonredundant data is 3136.

In Section 4.4 a denser antenna configuration (see Fig. 10) comprising 10512 nonredundant data is described and tested as well. Note that all measurement positions in Section 4 lie within a distance of 15 cm from the origin, hence they are in the reactive zone for both phantoms — the far field distances are approximately 1.9 m and 1.3 m for the class 1 and class 2 phantom reconstruction domains, respectively. As a consequence the estimate for the number of degrees of freedom (NDF) as given in [69] is not applicable here. Let us apply the estimate from [69] anyway as an indication: for the class 1 phantom it yields approximately 250 antenna positions evenly distributed over a sphere (in the far field), corresponding with NDF ≈ 125000; for the class 2 phantom it gives approximately 170 antenna positions and NDF ≈ 57800. It is clear that the numbers of nonredundant data employed in this paper are much lower than these estimates.
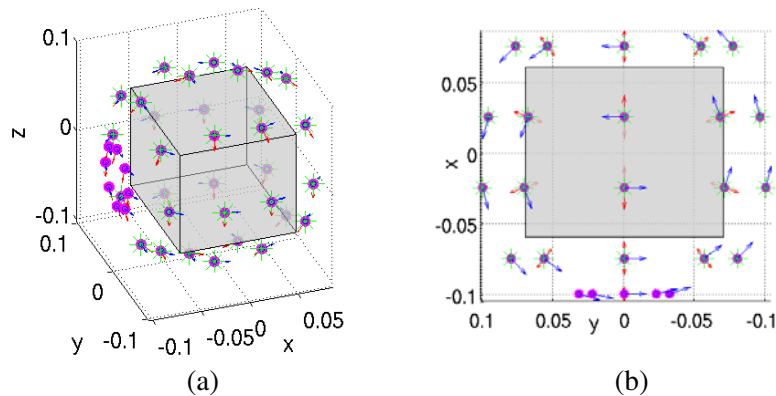
Figure 3. A sparse antenna configuration yielding $N^d = 5120$ data (3136 nonredundant data) employed in Sections 4.1–4.3: (a) xyz-view and (b) xy-view. Dots indicate antenna positions, green markers transmitting positions and arrows in two orthogonal directions the dipoles around a cuboid reconstruction domain. Axes are in m.

3.3. Some Parameters from the Literature

Note that in [3] and [37, 39] only x-directed antennas are used. Furthermore, their algorithms allow for smaller distances between a cylindrical measurement surface and a breast surface, since the reconstruction domain also is cylindrical; their antennas are more closely spaced on smaller measurement surfaces than with the configurations in this paper. For the reconstructions from clinical data in [3] the reconstruction domain is a cylinder with diameter 14 cm and height 5 cm, hence its volume ($\approx 770 \, \text{cm}^3$) is about 1.3 to 2.2 times smaller than the volumes we use in Section 4; a 15 cm diameter [32] circular 16-element array with antenna spacing $0.65\lambda_{b,[3]}$ ($\lambda_{b,[3]} \approx 4.5 \, \text{cm}$) is moved along x to 7 positions spaced apart 5 mm ($\approx 0.1\lambda_{b,[3]}$) spanning 3 cm, yielding 1680 complex data at 1.3 GHz; this number of data is about one third of our number $N^d = 5120$, but the number of 4500 reconstruction variables ($\approx 5.5 \, \text{mm}$ cell size) in [3] is also one third or a smaller fraction of the number $13440 \le N^\varepsilon \le 107520$ that we employ in Section 4. For the reconstructions of class 1 and class 2 phantoms, similar to the ones used in this paper, [37, 39, 40] adopt a 2 mm cell size within a reconstruction domain defined by the known breast contours, yielding 120000–360000 unknowns [39]; they employ a 40 element antenna array that consists of 5 ellipses spaced apart 1 cm and with an approximate diameter of 11 cm, each with 8 electrically-small dipoles spaced apart approximately 4.5 cm, yielding 1560 time domain signals.

4. RECONSTRUCTION RESULTS

In Section 4.1 we compare reconstructions obtained with Huber (6) and MS (Section 2.2) regularization for the class 1 phantom with a 2 cm tumor and the class 2 phantom with a 1.6 cm tumor from Fig. 2. We then continue with Huber regularization. We show some more examples for class 1 phantoms with a 2 cm tumor in different positions and with two tumors in Section 4.2. Finally we show reconstructions for smaller tumors in Section 4.3 and we compare with results obtained from a denser antenna configuration in Section 4.4. Unless otherwise specified, all reconstructions are performed on an inversion grid that is coarser than the data generation grid. We use this inversion grid also for the forward problem solutions during the reconstruction. The initial guess is equal to the background permittivity ε_b everywhere in the cuboid $\mathcal{D}$, hence we do not use prior knowledge of the breast contour as in [37, 39]. The tolerance for the BiCGSTAB routine is 10^{-3} everywhere in this Section. The permittivity bounds are $1.0 < \text{Re}(\varepsilon) < 55.0$ and $-50.0 < \text{Im}(\varepsilon) < 1.0$. We set the parameters $\mu = 1 \times 10^{-5}$ and $\gamma = 0.001$ for Huber regularization [42, 51]. For MS regularization we use $\mu = 1 \times 10^{-4}$ (this choice is not so critical). The iterations are stopped when the data error shows reductions less than 1%. All computations were performed on a six-core Intel i7 980x processor (3.33 GHz) with 24 GByte memory. Since for none of the reconstructions the real part of the permittivity attained values higher than 40, we employ the

scale $[1, 40]$ in the figures rather than $[1, 55]$ from Fig. 2; for the imaginary part the same scale as in Fig. 2 is used.

4.1. Reconstructions with Different Regularization Methods

4.1.1. Class 1 Breast Phantom

The diameter of the tumor is $2\,\text{cm}$ ($\approx \lambda_b/2.4$), see Figs. 2(a)–(d). The reconstruction grid $\mathcal{D}$ has dimensions $12\,\text{cm} \times 14\,\text{cm} \times 10\,\text{cm} = 1680\,\text{cm}^3$ and counts $24 \times 28 \times 20$ cells with size $5\,\text{mm}$ ($\approx 0.11\lambda_b$); the number of complex permittivity unknowns $N^\varepsilon = 13440$ is about 4 times as large as the number of nonredundant data. We noticed that convergence for both MS and Huber regularization occurred before 9 iterations. The reconstructions after 9 iterations (40 minutes — we did not optimize computation
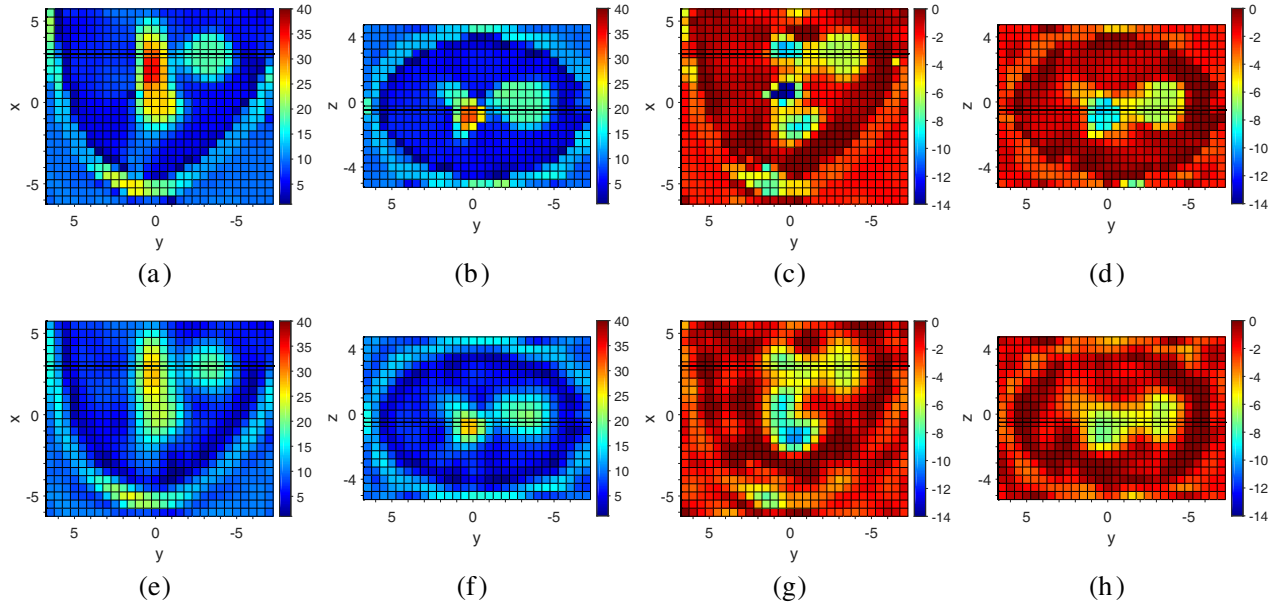
Figure 4. Complex permittivity reconstructions of the class 1 phantom from Fig. 2 with a $2.0\,\text{cm}$ diameter tumor at $(3\,\text{cm}, -3\,\text{cm}, 0\,\text{cm})$, obtained with (a)–(d) Huber regularization and (e)–(h) MS regularization. (a), (c), (e), (g) Sagittal slice near $z = 0\,\text{cm}$ and (b), (d), (f), (h) coronal slice near $x = 3\,\text{cm}$. (a), (b), (e), (f) Real part and (c), (d), (g), (h) imaginary part. A horizontal black line indicates the intersection of sagittal and coronal slices. The cell size is $5\,\text{mm}$. Axes are in cm. $N^d = 5120$ and SNR $= 20\,\text{dB}$.
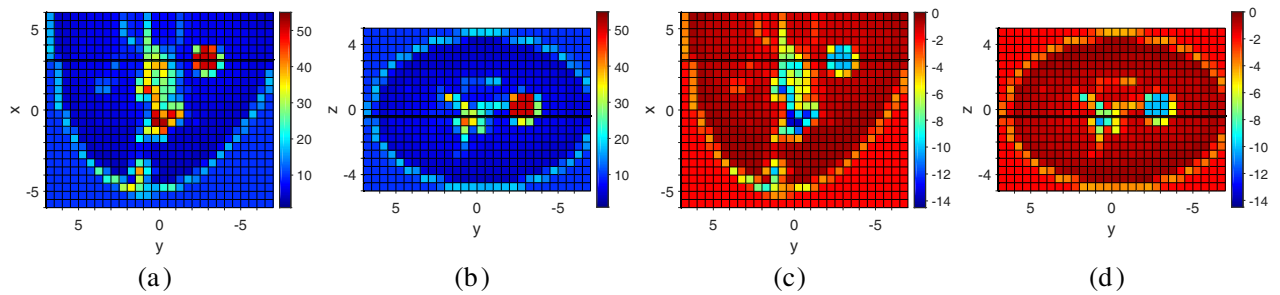

Figure 5. The complex permittivity in slices through a $5\,\text{mm}$ cell size locally averaged version of the discretized class 1 phantom of Figs. 2(a)–(d); this phantom does not serve for data generation, but as a visual reference for the reconstructions of Fig. 4. (a), (c) Sagittal slice near $z = 0\,\text{cm}$ and (b), (d) coronal slice near $x = 3\,\text{cm}$. (a), (b) Real part and (c), (d) imaginary part. A horizontal black line indicates the intersection of sagittal and coronal slices. Axes are in cm.

times) are depicted in Fig. 4, which shows the real and imaginary parts of the complex permittivity in nearly the same sagittal and coronal slices as with the exact phantom of Fig. 2 for the Huber (top row) and MS (bottom row) regularizations. The breast contour and the locations and dimensions of the healthy heterogeneities in the center and near the nipple and of the tumor are reconstructed in all images; the dimensions of the tumor are somewhat overestimated with the Huber method but it is clear from Figs. 4(a)–(d) that the tumor is better delineated than in the MS images from Figs. 4(e)–(h), which are more smoothed. The real part of the glandular tissues is underestimated for all images, but more for MS — an underestimation is also visible in Fig. 9 of [40]; some higher values ($\varepsilon' \approx 35$) are visible in the glandular tissues nearby the tumor with the Huber function. For the imaginary part of the glandular tissues, we also see some high absolute values in the Huber images. With both methods the maximum permittivity values of the tumor are similar (approximately $20 - j6.7$) and underestimated (exact value: $50 - j10$) but significantly higher than the surrounding adipose permittivity; the relative error of this maximum tumor permittivity is smaller for the imaginary part (33%) than for the real part (60%).

Finally we computed the RMS errors for both reconstructions with respect to the 5 mm cell size locally averaged version of the exact phantom of Figs. 2(a)–(d) shown in Fig. 5, where MS stands for the mean value of the squared differences over all cells in $\mathcal{D}$. These errors are quasi identical for the real parts (2.955 for Huber and 2.947 for MS regularization) and show a reduction of 8% for Huber relative to MS regularization for the imaginary parts (1.01 for Huber and 1.09 for MS regularization). Even though the RMS errors are quite similar for both methods, it is clear from a visual inspection that Huber regularization preserves better the sharpness of the details of interest.

4.1.2. Class 2 Breast Phantom

The diameter of the tumor is 1.6 cm ($\approx \lambda_b/3$) for this smaller phantom, see Figs. 2(e)–(h). The reconstruction grid $\mathcal{D}$ is a cube with size 10 cm and counts $25 \times 25 \times 25$ cells with size 4 mm ($\approx 0.08\lambda_b$),
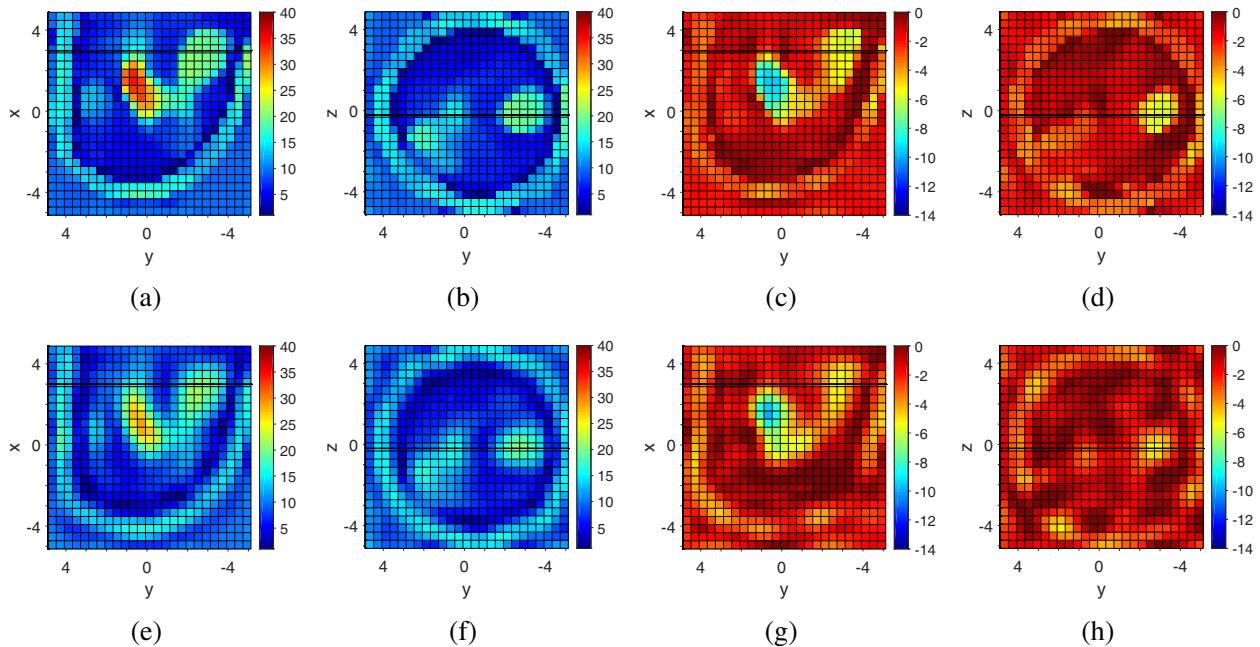
Figure 6. Complex permittivity reconstructions of the class 2 phantom from Fig. 2 with a 1.6 cm diameter tumor at (3 cm, −3 cm, 0 cm), obtained with (a)–(d) Huber regularization and (e)–(h) MS regularization. (a), (c), (e), (g) Sagittal slice near $z = 0$ cm and (b), (d), (f), (h) coronal slice near $x = 3$ cm. (a), (b), (e), (f) Real part and (c), (d), (g), (h) imaginary part. A horizontal black line indicates the intersection of sagittal and coronal slices. The cell size is 4 mm. Axes are in cm. $N^d = 5120$ and SNR = 20 dB.
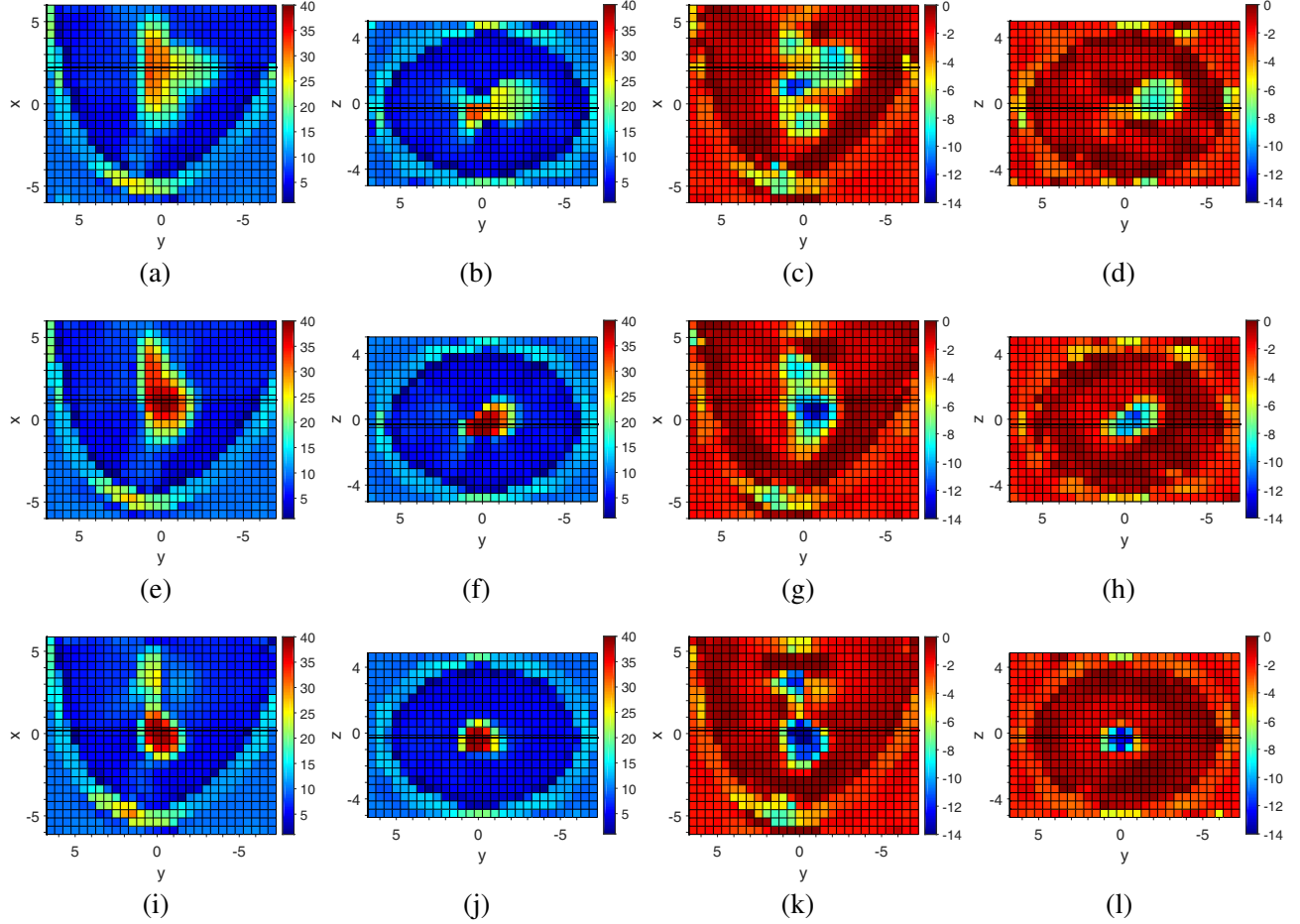
Figure 7. Complex permittivity reconstructions with Huber regularization of class 1 phantoms with a 2.0 cm diameter tumor at different positions in the xy-plane: tumor centered (a)–(d) at (2 cm, -2 cm, 0 cm), (e)–(h) at (1 cm, -1 cm, 0 cm) and (i)–(l) at (0 cm, 0 cm, 0 cm). (a), (c), (e), (g), (i), (k) Sagittal slice near $z = 0$ cm and (b), (d) coronal slices through the tumor at $x = 2.2$ cm, (f), (h) at $x = 1.2$ cm and (j), (l) at $x = 0.2$ cm. (a), (b), (e), (f), (i), (j) Real part and (c), (d), (g), (h), (k), (l) imaginary part. A horizontal black line indicates the intersection of sagittal and coronal slices. The cell size is 5 mm. Axes are in cm. $N^d = 5120$ and SNR $= 20$ dB.

hence the number of complex permittivity unknowns is $N^\varepsilon = 15625$. The results after 9 iterations are depicted in Fig. 6. The MS images are again more smoothed; the visibility of the tumor in the MS imaginary part now is weaker than with the larger tumor in the class 1 phantom. With the Huber images the tumor is clearly visible at the correct location and the average permittivity values of the central fibroglandular heterogeneity are rather well reconstructed, in particular for the imaginary part. As with the class 1 phantom the maximum permittivity values of the tumor (approximately $21 - j6.3$) are underestimated (exact value: $50 - j10$); the relative error of this maximum tumor permittivity is 37% for the imaginary part and 58% for the real part.

4.2. Different Tumor Positions and Multiple Tumors

We first let the 2 cm diameter tumor move from the original position (3 cm, -3 cm, 0 cm) in the class 1 phantom in Fig. 2 along a diagonal in the xy-plane to the center of the grid, yielding the positions (2 cm, -2 cm, 0 cm), (1 cm, -1 cm, 0 cm) and (0 cm, 0 cm, 0 cm). The same inversion grid as before with cell size 5 mm is employed. From the imaginary part in the reconstruction of Fig. 7(c) we notice that the tumor is clearly visible to the right of the glandular tissues at (2 cm, -2 cm, 0) and that its

value (≈ -9) is close to the actual value (-10); the real part is approximately 22. As the tumor is moved closer to the center of the grid, overlapping more and more with the original glandular tissues, its maximum permittivity in Fig. 7 (middle and bottom rows) changes to approximately ($40 - j14$) (exact value: $50 - j10$); the relative error of this maximum tumor permittivity is 40% for the imaginary part and 20% for the real part.

We now consider a class 1 phantom as in Fig. 2 and we insert an identical tumor to the left of the central tissues at ($3\,\text{cm}, 3\,\text{cm}, 0\,\text{cm}$). From the reconstructions in Fig. 8 we notice that both tumors are correctly located and that the reconstruction quality is not degraded by the additional tumor; the tumor values even are slightly better than those in Fig. 4 with maximum values of approximately $20 - j7.5$ for the right and $24 - j8.9$ for the left tumor; the relative errors of these maximum tumor permittivities are 25% and 11% for the imaginary parts and 60% and 52% for the real parts, respectively.

From Sections 4.1 and 4.2 we conclude that a (high permittivity) 2 cm tumor can be clearly (visually) distinguished within (low permittivity) adipose tissue, although its reconstructed permittivity values are lower than the actual ones. Such tumor is less distinguishable within (high permittivity) glandular tissues; the reconstructed values at its location then are closer to the actual ones.
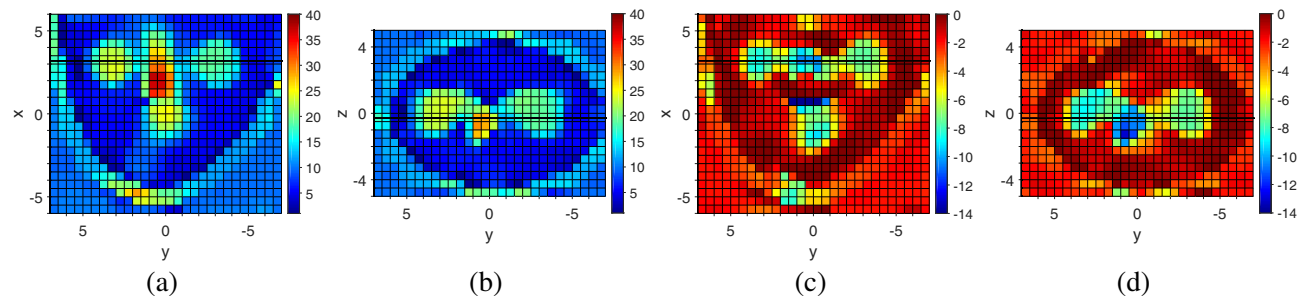

Figure 8. Complex permittivity reconstruction with Huber regularization of a class 1 phantom with two 2.0 cm diameter tumors centered at ($3\,\text{cm}, -3\,\text{cm}, 0\,\text{cm}$) and ($3\,\text{cm}, 3\,\text{cm}, 0\,\text{cm}$) in the xy-plane. (a), (c) Sagittal slice near $z = 0\,\text{cm}$ and (b), (d) coronal slice near $x = 3\,\text{cm}$. (a), (b) Real part and (c), (d) imaginary part. A horizontal black line indicates the intersection of sagittal and coronal slices. The cell size is 5 mm. Axes are in cm. $N^d = 5120$ and SNR $= 20\,\text{dB}$.

4.3. Smaller Tumor Sizes

We consider class 1 phantoms with a single tumor positioned in ($3\,\text{cm}, -3\,\text{cm}, 0\,\text{cm}$) with a diameter: $2.0\,\text{cm}$ ($\approx \lambda_b/2.4$), $1.6\,\text{cm}$ ($\approx \lambda_b/3$), $1.4\,\text{cm}$ ($\approx \lambda_b/3.4$) and $1.2\,\text{cm}$ ($\approx \lambda_b/4$). The equivalent diameters corresponding with the ($2.5\,\text{mm}$ cells) discretized tumor volumes respectively are $1.97\,\text{cm}$, $1.64\,\text{cm}$, $1.34\,\text{cm}$ and $1.19\,\text{cm}$. We used 5120 data from the antenna configuration of Fig. 3. Sagittal slices of the reconstructions with a cell size of 5 mm ($N^\varepsilon = 13440$) are shown in the top two rows of Fig. 9. We also did reconstructions with a cell size of 2.5 mm ($N^\varepsilon = 107520$), see the other rows of Fig. 9, where we employed the same values for the BiCGSTAB routine tolerance and the parameters μ and γ as before. We notice lower glandular permittivity (absolute) values with the 2.5 mm cell size than with the 5 mm cell size reconstructions; this might be due to the increased weight of the regularization term relative to the data error in (2), given the larger number of cells in the summation (5). It can be seen that the 1.6 cm diameter tumor is reconstructed at the right location in Fig. 9(b), but where the 2.0 cm diameter tumor in Fig. 9(a) is a bit oversized, this smaller one is a bit undersized. When the diameter decreases to 1.4 cm, only a faint change with respect to the surrounding permittivity is observed at the tumor location in Fig. 9(c) for the 5 mm cell size and in the 3D iso-surface; the tumor with diameter 1.2 cm is not visible in Fig. 9(d). Differential imaging techniques can be applied to resolve "invisible" tumors [37, 39]. Note further that the small lump — approximately 1 cm in Fig. 2(a) — of glandular tissue near the nipple is not resolved, but that the permittivity (absolute) values are significantly higher around the nipple. More simulations to study the influence of the tumor position and of the surrounding tissues and to fine tune regularization and computational parameters are needed to gain more insight into the reconstruction of small tumors.
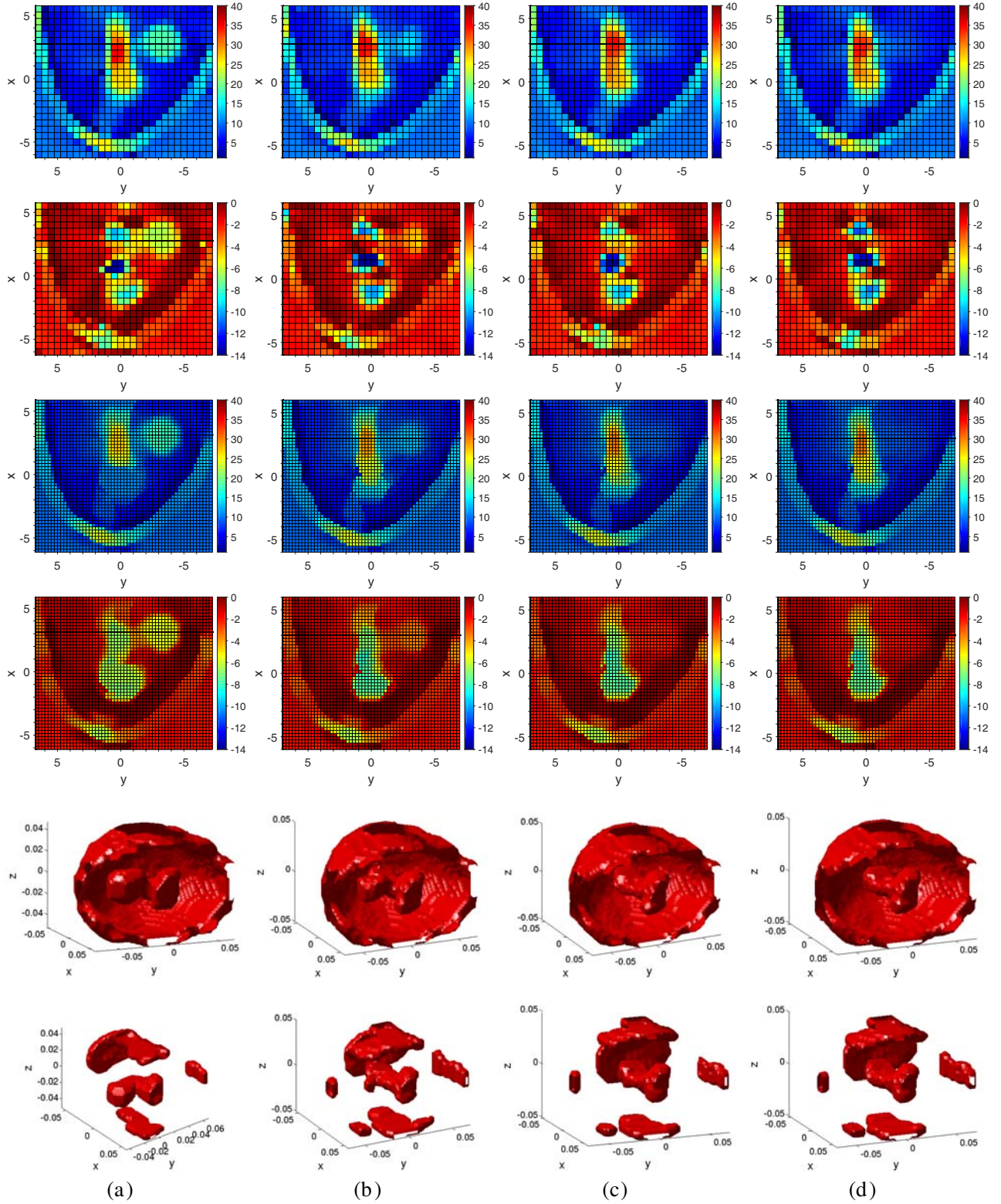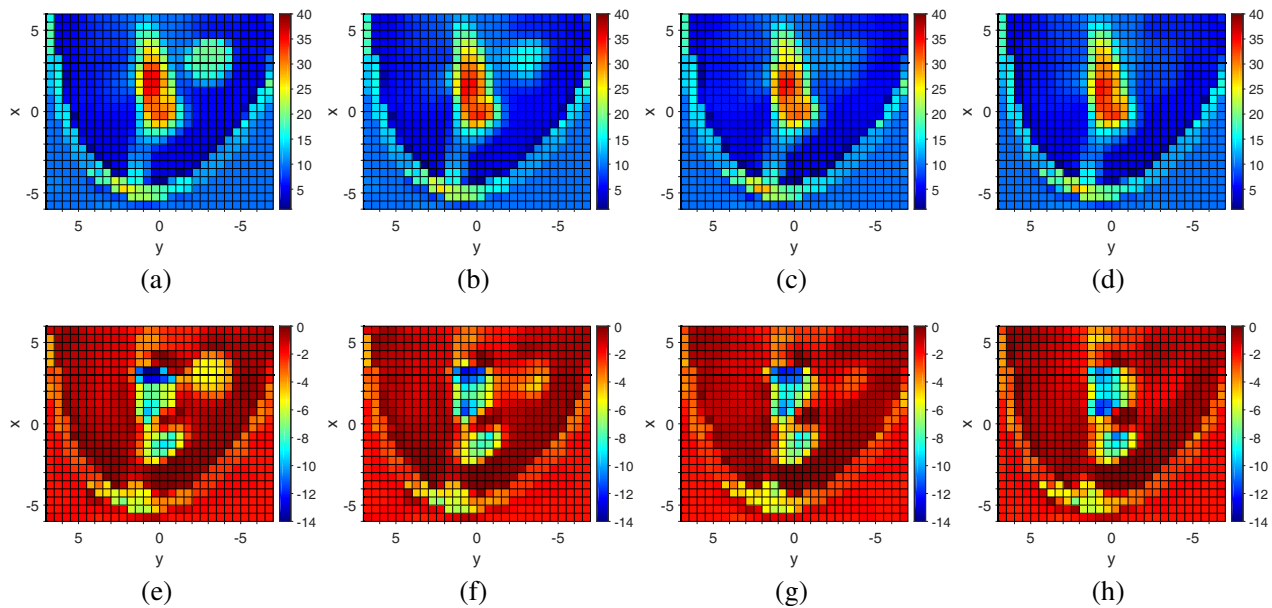
Figure 9. Complex permittivity reconstructions with Huber regularization of class 1 phantoms with different tumor diameters: (a) 20 mm, (b) 16 mm, (c) 14 mm and (d) 12 mm. Top 2 rows: (upper) real part and (lower) imaginary part for a 5 mm cell size; middle 2 rows: (upper) real part and (lower) imaginary part for a 2.5 mm cell size; axes are in cm. Bottom 2 rows: 3D iso-surfaces of the (upper) real part and (lower) imaginary part; axes are in m. $N^d = 5120$ and SNR = 20 dB.
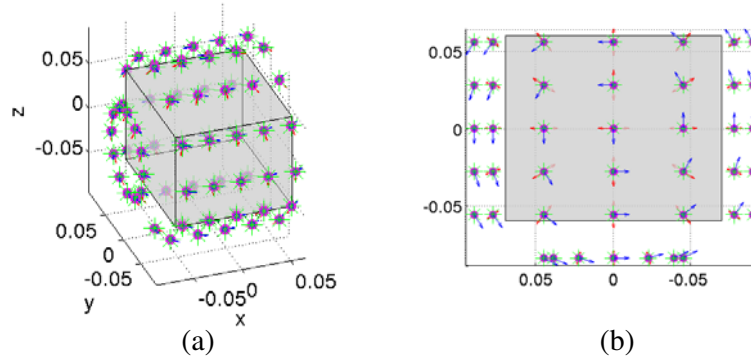
Figure 10. A denser antenna configuration yielding $N^d = 20736$ data (10512 nonredundant data) employed in Section 4.4: (a) xyz-view and (b) xy-view. Dots indicate antenna positions, green markers transmitting positions and arrows in two orthogonal directions the dipoles around a cuboid reconstruction domain. Axes are in m.

4.4. Reconstructions with a Denser Antenna Array

We show reconstructions for phantoms with similar tumors as in Section 4.3, but these phantoms were obtained from the high resolution phantom by applying a local averaging cell size of 4 mm. The equivalent tumor diameters corresponding with the (4 mm cells) discretized tumor volumes are 1.90 cm, 1.64 cm, 1.35 cm and 1.14 cm. We used a more dense antenna configuration than with the previous reconstructions, see Fig. 10. It consists of 5 circles with diameter 18 cm and one smaller circle with diameter 9 cm, spaced 2.8 cm ($\approx 0.6\lambda_b$) in the x-direction. The small circle is at $x = -8.4$ cm in front of the nipple and the last circle is at $x = 5.6$ cm at the chest wall. There are 12 antenna positions on each circle, spaced 4.7 cm ($\approx \lambda_b$) for the large circles, yielding 72 positions in total, and 2 polarizations per position. We used all positions for transmitting and receiving, hence the number of complex field data is $N^d = 20736$, which is 4 times the number of data used before. Note that nearly half of these

Figure 11. Complex permittivity reconstructions with Huber regularization of class 1 phantoms with different tumor sizes and using $N^d = 20736$ field data from Fig. 10: (top row) real part and (bottom row) imaginary part. The tumor diameters are (a), (e) 20 mm, (b), (f) 16 mm, (c), (g) 14 mm and (d), (h) 12 mm. The cell size is 5 mm. SNR = 20 dB.

data are redundant due to reciprocity, yielding 10512 nonredundant data.

We used a 5 mm cell size for the reconstructions, hence $N^\varepsilon = 13440$. This number is still larger than the number of nonredundant data. The images after 12 iterations are shown in Fig. 11. By comparing Fig. 11 with Fig. 9 we notice some small changes: the shape and permittivity values of the central glandular tissues in Fig. 11 are a bit closer to the exact phantom; the lump of glandular tissue near the nipple now is appearing faintly in the real part; the absolute value of the imaginary part of the 2.0 cm diameter tumor in Fig. 11(a) is a bit lower (≈ 5.5) than before; the 1.6 cm diameter tumor in Fig. 11(b) is less undersized and the presence of the 1.4 cm diameter tumor in Fig. 11(c) is a bit more pronounced than before; the smallest tumor in Fig. 11(d) is still not visible. Since we used different data generation models in Sections 4.3 and 4.4 it is possible that these changes are not entirely due to the larger amount of data. More simulations, e.g., with smaller cell sizes, more closely spaced receiving antennas, are needed to further investigate the reconstruction of small tumors.

5. CONCLUSIONS

In this paper we employed the Huber function in the regularization term in the nonlinear cost function for 3D quantitative microwave breast imaging. An iterative Gauss-Newton optimization scheme with constrained line-searches was applied. We showed complex permittivity reconstructions from synthetic bi-polarized scattered field data at 2 GHz for two types of breast phantoms with one (and two) tumor(s), that we adapted from the UWCEM online repository. The number of nonredundant field data was significantly lower than the number of reconstruction voxels and a SNR of 20 dB was adopted. The Huber regularization was more effective in preserving the edges of the different tissues when compared to a quadratic smoothing regularization. Tumors with diameters 2 cm and 1.6 cm were clearly visible and correctly located in the reconstructed images, but the real parts of their permittivity values were approximately between 20% and 60% too low and the imaginary parts showed differences between 10% and 35% with respect to the actual values. A smaller 1.2 cm diameter tumor was not visible in the reconstruction, also not when the number of nonredundant data was increased from 23% to 78% of the number of voxels. A further improvement of these reconstructions could possibly result from optimizing a number of computational parameters and from using more closely spaced receiving antennas.

ACKNOWLEDGMENT

REFERENCES

1. Joines, W. T., Y. Zhang, C. Li, and R. L. Jirtle, "The measured electrical properties of normal and malignant human tissues from 50 to 900 MHz," *Med. Phys.*, Vol. 21, No. 4, 547–550, 1994.

2. Lazebnik, M. D., et al., "A large-scale study of the ultrawideband microwave dielectric properties of normal, benign and malignant breast tissues obtained from cancer surgeries," *Phys. Med. Biol.*, Vol. 52, No. 20, 6093–6115, 2007.

3. Grzegorczyk, T. M., et al., "Fast 3D tomographic microwave imaging for breast cancer detection," *IEEE Trans. Med. Imaging*, Vol. 31, No. 8, 1584–1592, 2012.

4. Larsen, L. E. and J. H. Jacobi, "Microwave scattering parameter imagery of an isolated canine kidney," *Med. Phys.*, Vol. 6, No. 5, 394–403, 1979.

5. Pichot, C., L. Jofre, G. Peronnet, and J.-C. Bolomey, "Active microwave imaging of inhomogeneous bodies," *IEEE Trans. Antennas Propag.*, Vol. 33, No. 4, 416–425, 1985.

6. Jofre, L., et al., "Medical imaging with a microwave tomographic scanner," *IEEE Trans. Biomed. Eng.*, Vol. 37, No. 3, 303–312, 1990.

7. Li, X., E. J. Bond, B. D. Van Veen, and S. C. Hagness, "An overview of ultra-wideband microwave imaging via space-time beamforming for early-stage breast-cancer detection," *IEEE Antennas Propag. Mag.*, Vol. 47, No. 1, 19–34, 2005.

8. Klemm, M., et al., "Radar-based breast cancer detection using a hemispherical antenna array — Experimental results," *IEEE Trans. Antennas Propag.*, Vol. 57, No. 6, 1692–1704, 2009.

9. Porter, E., A. Santorelli, and M. Popovic, "Time-domain microwave radar applied to breast imaging: Measurement reliability in a clinical setting," *Progress In Electromagnetics Research*, Vol. 149, 119–132, 2014.

10. De Zaeytijd, J., C. Conmeaux, and A. Franchois, "Three-dimensional linear sampling applied to microwave breast imaging," *Proc. XXIXth URSI General Assembly*, Chicago, Aug. 7–16, 2008.

11. Chew, W. C. and Y. M. Wang, "Reconstruction of two-dimensional permittivity distribution using the distorted born iterative method," *IEEE Trans. Med. Imaging*, Vol. 9, No. 2, 218–225, 1990.

12. Kleinman, R. E. and P. M. van den Berg, "A modified gradient method for two-dimensional problems in tomography," *J. Comput. Appl. Math.*, Vol. 42, 17–35, 1992.

13. Joachimowicz, N., C. Pichot, and J.-P. Hugonin, "Inverse scattering: An iterative numerical method for electromagnetic imaging," *IEEE Trans. Antennas Propag.*, Vol. 39, No. 12, 1742–1752, 1991.

14. Meaney, P. M., K. D. Paulsen, and T. P. Ryan, "Two-dimensional hybrid element image reconstruction for TM illumination," *IEEE Trans. Antennas Propag.*, Vol. 43, No. 3, 239–247, 1995.

15. Franchois, A. and C. Pichot, "Microwave imaging-complex permittivity reconstruction with a Levenberg-Marquardt method," *IEEE Trans. Antennas Propag.*, Vol. 45, 203–215, 1997.

16. Abubakar, A., P. M. van den Berg, and J. J. Mallorqui, "Imaging of biomedical data using a multiplicative regularized contrast source inversion Method," *IEEE Trans. Microw. Theory Tech.*, Vol. 50, No. 7, 1761–1771, 2002.

17. Zhang, Z. Q. and Q. H. Liu, "Three-Dimensional nonlinear image reconstruction for microwave biomedical imaging," *IEEE Trans. Biomed. Eng.*, Vol. 51, No. 3, 544–548, 2004.

18. Bulyshev, A. E., et al., "Three-dimensional vector microwave tomography: Theory and computational experiments," *Inverse Probl.*, Vol. 20, No. 4, 1239–1259, 2004.

19. De Zaeytijd, J., A. Franchois, C. Eyraud, and J.-M. Geffrin, "Full-wave three-dimensional microwave imaging with a regularized Gauss-Newton method — Theory and experiment," *IEEE Trans. Antennas Propag.*, Vol. 55, No. 11, 3279–3292, 2007.

20. Takenaka, T., H. Zhou, and T. Tanaka, "Inverse scattering for a three-dimensional object in the time domain," *J. Opt. Soc. Am. A*, Vol. 20, No. 10, 1867–1874, 2003.

21. Rekanos, I. T., "Time-domain inverse scattering using Lagrange multipliers: An iterative FDTD-based optimization technique," *Journal of Electromagnetic Waves and Applications*, Vol. 17, No. 2, 271–289, 2003.

22. Fhager, A., P. Hashemzadeh, and M. Persson, "Reconstruction quality and spectral content of an electromagnetic time-domain inversion algorithm," *IEEE Trans. Biomed. Eng.*, Vol. 53, No. 8, 1594–1604, 2006.

23. Meaney, P. M., K. D. Paulsen, A. Hartov, and R. K. Crane, "Microwave imaging for tissue assessment: Initial evaluation in multitarget tissue-equivalent phantoms," *IEEE Trans. Biomed. Eng.*, Vol. 43, No. 9, 878–890, 1996.

24. Franchois, A., A. Joisel, C. Pichot, and J.-C. Bolomey, "Quantitative microwave imaging with a 2.45-GHz planar microwave camera," *IEEE Trans. Med. Imaging*, Vol. 17, No. 4, 550–561, 1998.

25. Joachimowicz, N., J. J. Mallorqui, J.-C. Bolomey, and A. Broquetas, "Convergence and stability assessment of Newton-Kantorovich reconstruction algorithms for microwave tomography," *IEEE Trans. Med. Imaging*, Vol. 17 No. 4, 562–570, 1998.

26. Mojabi, P. and J. LoVetri, "Microwave biomedical imaging using the multiplicative regularized Gauss-Newton inversion," *IEEE Ant. Wireless Prop. Lett.*, Vol. 8, 645–648, 2009.

27. Fhager, A., M. Gustafsson, and S. Nordebo, "Image reconstruction in microwave tomography using a dielectric Debye model," *IEEE Trans. Biomed. Eng.*, Vol. 59, No. 1, 156–166, 2012.

28. Semenov, S. Y., et al., "Three-dimensional microwave tomography: Initial experimental imaging of animals," *IEEE Trans. Biomed. Eng.*, Vol. 49, No. 1, 55–63, 2002.

29. Yu, C., et al., "Active microwave imaging II: 3-D system prototype and image reconstruction from experimental data," *IEEE Trans. Microw. Theory Tech.*, Vol. 56, No. 4, 991–1000, 2008.

30. Abubakar, A., T. M. Habashy, G. Pan, and M.-K. Li, "Application of the multiplicative regularized Gauss-Newton algorithm for three-dimensional microwave imaging," *IEEE Trans. Antennas Propag.*, Vol. 60, No. 5, 2431–2441, 2012.

31. Catapano, I., L. Di Donato, L. Crocco, and O. M. Bucci, A. F. Morabito, T. Isernia, and R. Massa, "On quantitative microwave tomography of female breast," *Progress In Electromagnetics Research*, Vol. 97, 75–93, 2009.

32. Meaney, P. M., et al., "A clinical prototype for active microwave imaging of the breast," *IEEE Trans. Microw. Theory Tech.*, Vol. 48, No. 11, 1841–1853, 2000.

33. Rubaek, T., P. M. Meaney, P. Meincke, and K. D. Paulsen, "Nonlinear microwave imaging for breast-cancer screening using Gauss-Newton's method and the CGLS inversion algorithm," *IEEE Trans. Antennas Propag.*, Vol. 55, No. 8, 2320–2331, 2007.

34. Henriksson, T., et al., "Quantitative microwave imaging for breast cancer detection using a planar 2.45 GHz system," *IEEE Trans. Instrum. Meas.*, Vol. 59, No. 10, 2691–2699, 2010.

35. Bulyshev, A. E., et al., "Computational modeling of three-dimensional microwave tomography of breast cancer," *IEEE Trans. Biomed. Eng.*, Vol. 48, No. 9, 1053–1056, 2001.

36. Zhou, H., T. Takenaka, J. E. Johnson, and T. Tanaka, "A breast imaging model using microwaves and a time domain three dimensional reconstruction method," *Progress In Electromagnetics Research*, Vol. 93, 57–70, 2009.

37. Winters, D. W., J. D. Shea, P. Kosmas, B. D. Van Veen, and S. C. Hagness, "Three-dimensional microwave breast imaging: Dispersive dielectric properties estimation using patient-specific basis functions," *IEEE Trans. Med. Imaging*, Vol. 28, No. 7, 969–981, 2009.

38. Winters, D. W., et al., "A sparsity regularization approach to the electromagnetic inverse scattering problem," *IEEE Trans. Antennas Propag.*, Vol. 58, No. 1, 145–154, 2010.

39. Shea, J. D., P. Kosmas, B. D. Van Veen, and S. C. Hagness, "Contrast-enhanced microwave imaging of breast tumors: A computational study using 3D realistic numerical phantoms," *Inverse Probl.*, Vol. 26, No. 7, Article ID 074009, 2010.

40. Shea, J. D., P. Kosmas, S. C. Hagness, and B. D. Van Veen, "Three-dimensional microwave imaging of realistic numerical breast phantoms via a multiple-frequency inverse scattering technique," *Med. Phys.*, Vol. 37, No. 8, 4210–4226, 2010.

41. De Zaeytijd, J., "On the 3D electromagnetic quantitative inverse scattering problem: Algorithms and regularization," Ph.D. thesis, Ghent University, 2009.

42. Bai, F., A. Franchois, J. De Zaeytijd, and A. Pižurica, "Three-dimensional quantitative microwave imaging of realistic numerical breast phantoms using Huber regularization," *Proc. 35th Annual Int. Conf. IEEE Eng. Med. Biol. Society (EMBS)*, 5135–5138, Osaka, Japan, Jul. 3–7, 2013.

43. De Zaeytijd, J. and A. Franchois, "A subspace preconditioned LSQR Gauss-Newton method with a constrained linesearch path applied to 3D biomedical microwave imaging," *Int. J. Antennas Propag.*, Article ID 924067, 2015.

44. Azghani, M., P. Kosmas, and F. Marvasti, "Fast microwave medical imaging based on iterative smoothed adaptive thresholding," *IEEE AWP Letters*, Vol. 14, 438–441, 2015.

45. Golnabi, A. H., et al., "Comparison of no-prior and soft-prior regularization in biomedical microwave imaging," *J. Med. Phys.*, Vol. 36, No. 3, 159–170, 2011.

46. Tijhuis, A. G., K. Belkebir, A. C. S. Litman, and B. P. De Hon, "Theoretical and computational aspects of 2-D inverse profiling," *IEEE Trans. Geosci. Remote Sens.*, Vol. 39, 1316–1330, 2001.

47. Habashy, T. M. and A. Abubakar, "A general framework for constraint minimization for the inversion of electromagnetic measurements," *Progress In Electromagnetics Research*, Vol. 46, 265–312, 2004.

48. De Zaeytijd, J., A. Franchois, and J.-M. Geffrin, "A new value picking regularization strategy — Application to the 3-D electromagnetic inverse scattering problem," *IEEE Trans. Antennas Propag.*, Vol. 57, No. 4, 1133–1149, 2009.

49. Van den Bulcke, S., A. Franchois, and D. De Zutter, "Piecewise smoothed value picking regularization applied to 2-D TM and TE inverse scattering," *IEEE Trans. Antennas Propag.*, Vol. 61, No. 6, 3261–3269, 2013.

50. Bai, F., et al., "Weakly convex discontinuity adaptive regularization for microwave imaging," *IEEE Trans. Antennas Propag.*, Vol. 61, No. 12, 6242–6246, 2013.

51. Bai, F., et al., "Weakly convex discontinuity adaptive regularization for 3D quantitative microwave tomography," *Inverse Probl.*, Vol. 30, No. 8, Article ID 085005, 2014.

52. Lobel, P., L. Blanc-Féraud, Ch. Pichot, and M. Barlaud, "A new regularization scheme for inverse scattering," *Inverse Probl.*, Vol. 13, No. 2, 403–410, 1997.

53. Caorsi, S., G. L. Gragnani, S. Medicina, M. Pastorino, and G. Zunino, "Microwave imaging based on a Markov random field model," *IEEE Trans. Antennas Propag.*, Vol. 42, No. 3, 293–303, 1994.

54. Baussard, A., D. Prémel, and O. Venard, "A Bayesian approach for solving inverse scattering from microwave laboratory-controlled data," *Inverse Probl.*, Vol. 17, 1659–1669, 2001.

55. Ferraiuolo, G. and V. Pascazio, "The effect of modified markov random fields on the local minima occurrence in microwave imaging," *IEEE Trans. Geosci. Remote Sens.*, Vol. 41, 1043–1055, 2003.

56. De Zaeytijd, J. and A. Franchois, "Three-dimensional quantitative microwave imaging from measured data with multiplicative smoothing and value picking regularization, *Inverse Probl.*, Vol. 25, No. 2, 024004, 2009.

57. Li, S. Z., *Markov Random Field Modeling in Image Analysis*, Springer Publishing Company, Incorporated, New York City, USA, 1995.

58. Huber, P. J., "Robust estimation of a location parameter," *Ann. Math. Statist.*, Vol. 35, 73–101, 1964.

59. Schultz, R. R. and R. L. Stevenson, "A Bayesian approach to image expansion for improved definition," *IEEE Trans. Image Process.*, Vol. 3, No. 3, 233–242, 1994.

60. Geffrin, J.-M., P. Sabouroux, and C. Eyraud, "Free space experimental scattering database continuation: Experimental set-up and measurement precision," *Inverse Probl.*, Vol. 21, No. 6, S117, 2005.

61. Geffrin, J.-M. and P. Sabouroux, "Continuing with the Fresnel database: Experimental setup and improvements in 3D scattering measurements," *Inverse Probl.*, Vol. 25, No. 2, 024001, 2009.

62. Bai, F., "Spatial priors for tomographic reconstructions from limited data," Ph.D. thesis, Ghent University, 2014.

63. Zastrow, E., et al., "Database of 3D grid-based numerical breast phantoms for use in computational electromagnetics simulations," https://uwcem.ece.wisc.edu/MRIdatabase/InstructionManual.pdf.

64. De Zaeytijd, J., I. Bogaert, and A. Franchois, "An efficient hybrid MLFMA-FFT solver for the volume integral equation in case of sparse 3D inhomogeneous dielectric scatterers," *J. Comput. Phys.*, Vol. 227, No. 14, 7052–7068, 2008.

65. Chaumet, P. C. and K. Belkebir, "Three-dimensional reconstruction from real data using a conjugate gradient-coupled dipole method," *Inverse Probl.*, Vol. 25, No. 2, 024003, 2009.

66. Da Cunha, R. D. and T. Hopkins, "The parallel iterative methods (PIM) package for the solution of systems of linear equations on parallel computers," *Appl. Num. Math.*, Vol. 19, 33–50, 1995.

67. Fletcher, R., *Practical Methods of Optimization*, 2nd Edition, John Wiley, New York, NY, USA, 1990.

68. Zastrow, E., et al., "Development of anatomically realistic numerical breast phantoms with accurate dielectric properties for modeling microwave interactions with the human breast," *IEEE Trans. Biomed. Eng.*, Vol. 55, No. 12, 2792–2800, 2008.

69. Bucci, O. M. and T. Isernia, "Electromagnetic inverse scattering: retrievable information and measurement strategies," *Radio Sci.*, Vol. 32, 2123–2137, 1997.